Electrochimica Acta 433 (2022) 141262

Contents lists available at ScienceDirect

Electrochimica Acta

journal homepage: www.journals.elsevier.com/electrochimica-acta

# Ultrafast self-assembly $Fe_2O_3$ nanoparticles confined in carbon layers toward robust heterogeneous electro-Fenton reaction

Shuang Pan [a], Chang Liu [b], Yanchao Li [a], Can Wang [a,*], Xiaoya Cui [b], Ning Liu [a], Cong Zhang [a], Israel Hakizimana [a], Xin Zhao [a], Weidi Liu [c], Yanan Chen [b,*]

[a] School of Environmental Science and Engineering, Tianjin University, Tianjin 300350, China
[b] School of Materials Science and Engineering, Tianjin University, Tianjin 300072, China
[c] Australian Institute for Bioengineering and Nanotechnology, University of Queensland, St Lucia, QLD 4072, Australia

ARTICLE INFO

*Keywords:*
Heterogeneous electro-Fenton
Cathode fabrication
High-temperature shock
Methylisothiazolinone
Degradation mechanism

ABSTRACT

Heterogeneous electro-Fenton (EF) is a promising advanced oxidation process for refractory wastewater treatment. However, typical calcination or hydrothermal method for heterogeneous EF cathode fabrication is time-consuming, energy-consuming, or harmful to the environment. High-temperature shock (HTS) technique is a novel and rapid material synthesis method with the advantages of low-cost, eco-friendly. In this study, the electrodes named $Fe_2O_3$@C/carbon cloth ($Fe_2O_3$@C/CC), were synthesized by HTS for the first time within an extremely short time (~5 s). The $Fe_2O_3$ nanoparticles with an average diameter of 61.90 ± 15.09 nm are uniformly dispersed on carbon cloth (CC) with the confinement and protection of the carbon layers. The as-prepared $Fe_2O_3$@C/CC cathode exhibited excellent electrocatalytic properties in the EF system. The removal efficiency of methylisothiazolinone (MIT) could reach 90.60 ± 1.70% in 40 min at a low current density of 1.11 mA $cm^{-2}$ under the oxidation of the hydroxyl radical. In addition, the degradation pathways of MIT were further studied. According to the results of theoretical calculation, the –S–N– bond is the primary active site attacked during MIT degradation process. Therefore, heterocyclic loop opening is the main pathway of MIT degradation. HTS is an ultrafast and convenient potential technique compared with other cathode synthesis methods.

## 1. Introduction

As a promising electrochemical advanced oxidation process, electro-Fenton (EF) technology has attracted extensive attention in recent years [1–5]. In the EF process, gaseous oxygen obtains electrons to generate $H_2O_2$ at the cathode (named as oxygen reduction reaction, ORR, Eq. (1)), greatly reducing the risk of $H_2O_2$ transportation and storage [6]. Subsequently, the $H_2O_2$ generated by cathodes reacts with $Fe^{2+}$ catalyst to realize *in situ* production of HO· with nonselective oxidation capacity (Eq. (2)) [6], which can thereby shorten the transmission path of $H_2O_2$ and improve the mass transfer efficiency. $Fe^{3+}$ gains electron to complete the cycle with $Fe^{2+}$ (Eq. (3)) [7,8]. However, the conventional homogeneous EF process is realized by adding ferric catalysts into the system. This approach has the drawbacks of critical requirement of pH and iron mud pollution [9–12]. Many scholars built heterogeneous EF systems to overcome these shortcomings by fixing catalysts on cathodes or using solid carriers [13,14].

$$O_2+2e^-+2H^+\rightarrow H_2O_2 \quad (1)$$

$$H_2O_2+Fe^{2+}\rightarrow Fe^{3+}+HO\cdot+OH^- \quad (2)$$

$$Fe^{3+}+e^-\rightarrow Fe^{2+} \quad (3)$$

The cathode materials featured with abundant reactive sites are promising for efficient heterogeneous EF. The particle size, adhesion capacity, and uniform distribution of catalysts can considerably affect the reaction process. Therefore, the cathode preparation process plays a vital role in improving electrode properties. The commonly used cathode preparation processes of cathodes include impregnation [15], calcination [16,17], hydrothermal methods [3,14,18], electrostatic spinning [19], and roller pressing [2]. Li et al. prepared Fe@$Fe_2O_3$/active carbon fiber (Fe@$Fe_2O_3$/ACF) cathode via impregnation method, which showed high activity in degrading dye pollutant rhodamine B in water under neutral pH conditions [15]. Cui et al. synthesized Cu/Cu-$Fe_2O_4$-integrated graphite felt (Cu/Cu$Fe_2O_4$-CB@GF) as a stable

* Corresponding authors.
*E-mail addresses:* wangcan@tju.edu.cn (C. Wang), yananchen@tju.edu.cn (Y. Chen).

https://doi.org/10.1016/j.electacta.2022.141262
Received 16 June 2022; Received in revised form 14 September 2022; Accepted 26 September 2022
Available online 27 September 2022

bifunctional cathode with high stability and activity for heterogeneous EF oxidation via solvothermal reduction and calcination methods [16]. Although, these cathode preparation processes can successfully synthesize highly stable and active cathode materials by solvent reactions or heat treatments, these electrode preparation processes take more than a few or dozens of hours.

High-temperature shock (HTS) technology is a rapid, low-cost, and eco-friendly synthesis method that has been used in catalytic material preparation and nanomanufacturing in recent years [20,21]. As shown in Figs. 1 and 2(h), a large amount of joule heat is generated in a short period during the HTS process by applying ultrafast current or voltage pulse to the preinstalled materials in a vacuum chamber. The ultrafast heating and cooling processes promote the movement and rearrangement of atoms [22]. The precursors are reduced and decomposed to final products, *i.e.*, well-crystalline nanocatalysts, which are uniformly distributed on the substrate [23]. After the HTS process, the high-temperature samples can cool down within milliseconds. Chen et al. fabricated a conductive reduced graphene oxide (RGO) composite with silicon nanoparticles (NPs) using high-temperature radiative heating with excellent performance as a Li-ion battery anode [24]. Li et al. prepared nano-Ni@C/RGO *in situ* via the HTS process as a high-performance $H_2O_2$ fuel catalyst [25]. Moreover, the nanosized particles can be uniformly dispersed on the substrate with a strong bonding force under HTS conditions.

With the unique advantages of rapid reaction and formation of ultrafine catalyst, the HTS process can potentially introduce highly dispersed NPs into cathode materials leading to high catalytic performance. In this study, for the first time, we prepared the $Fe_2O_3$@C/carbon cloth ($Fe_2O_3$@C/CC) cathode by the ultrafast HTS technique and reported its application in heterogeneous EF oxidation. The morphology, structure, and electrochemical performance of the $Fe_2O_3$@C/CC cathode were characterized. Methylisothiazolinone (MIT) was chosen as a target contaminant because it is a commonly used fungicide with toxic risks and difficulty in biodegradation [26–28]. The degradation performance of MIT and the reaction mechanism of EF process were studied, and the suitability of the material as an EF cathode was proved. Finally, the degradation mechanism of MIT was discussed by analyzing the intermediate products and the theoretical calculation. This work confirms that the HTS is an ultrafast, feasible and energy-saving potential technique for preparing heterogeneous EF cathodes.

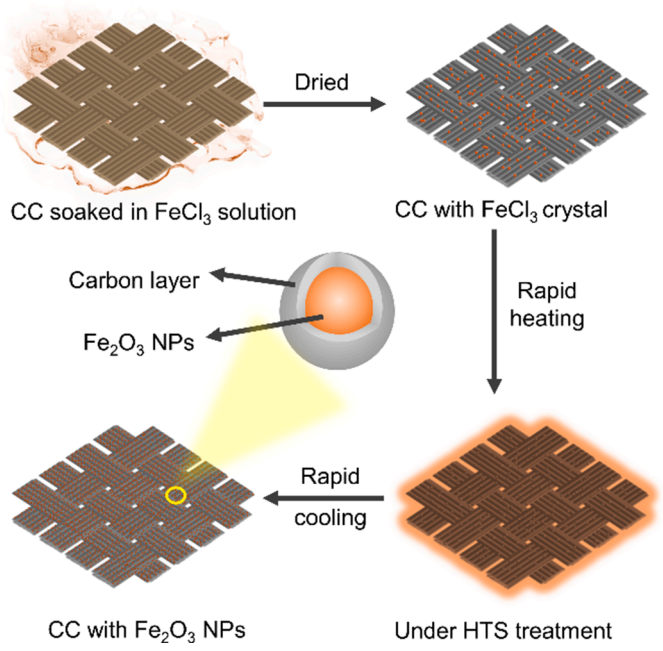


**Fig. 1.** Schematic illustration of the synthesis route of $Fe_2O_3$@C/CC.

## 2. Materials and methods

### 2.1. Materials and chemicals

The carbon cloth (CC) (W0S1011) was obtained from Cetech Co., Ltd. (Taiwan, China). Iron chloride hexahydrate ($FeCl_3{\cdot}6H_2O$, 99%, CAS: 10,025–77–1) was purchased from Damao Chemical Reagent (Tianjin, China). MIT (95%, CAS: 2682–20–4), tert-butanol (t-buOH, 99%, CAS: 75–65–0), and para-chlorobenzoic acid (pCBA, 99%, CAS: 74–11–3) were supplied by Aladdin Reagent (Shanghai, China). Other chemicals used in this work were analytical grade or higher.

### 2.2. Preparation of the cathode

The CC samples cut in 3 cm × 6 cm dimensions were first cleaned sequentially with acetone, ethanol, and ultrapure water to remove organic impurities, such as oil stains, and enhance electrical conductivity. Then, the precleaned CC was carbonized in a nitrogen atmosphere at 1073 K for 2 h using a horizontal tubular furnace.

The pretreated CC was soaked into the 50 mM $FeCl_3{\cdot}6H_2O$ ethanol solution for 0.5 h and dried in a vacuum drying oven. Then, the as-prepared electrode (named as $FeCl_3$/CC) was subjected to HTS treatment, as shown in Fig. 1. The details are depicted as follows: The $FeCl_3$/CC was clamped with a pair of graphite clips and placed on the heat shield in a vacuum acrylic box (Fig. S1). A stabilized DC power supply was connected to both ends of the graphite clips. A large amount of joule heat was generated in the $FeCl_3$/CC when the power was switched on, and the temperature could rise to more than 1373 K rapidly (Fig. 2(g)). After the power supply was cut off, the sample was cooled down within 5 s. In this process, microsized particles melt when heated and self-assemble into nanoparticles when cooled.

### 2.3. Material characterization and electrochemical measurements

The morphology images of the prepared cathodes were taken by Apreo S LoVac scanning electron microscope (SEM) and JEOL-1230 transmission electron microscope (TEM). The microstructure of samples was observed by a high-resolution transmission electron microscope (HRTEM, JEOL-JEM 2100F) and TEM mapping (Oxford 80T). The energy-dispersive X-ray spectroscopy (EDX) mapping was conducted by an Oxford EDX spectrometer (type X-Max80). The X-ray photoelectron spectroscopy (XPS) spectra were obtained by ESCALAB 250Xi of Thermo Fischer of America (C 1s = 284.8 eV).

All the electrochemical measurements were tested on the CHI660E electrochemical workstation (Shanghai, Chenhua, China) in a three-electrode cell, wherein the $Fe_2O_3$@C/CC or CC was a working electrode, and the Ag/AgCl electrode and Pt electrode were reference electrode and counter electrode, respectively. Linear sweep voltammetry (LSV) and chronoamperometry (CA) measurements were measured at room temperature (25 ± 1 °C) in 0.5 M $Na_2SO_4$ solution. Cyclic voltammetry (CV) was conducted in a 0.1 M potassium chloride (KCl) solution containing 10 mM potassium ferricyanide ($K_3[Fe(CN)_6]$). The electrochemical impedance spectroscopy (EIS) was conducted at a potential of 1.5 V in a frequency range from 100 kHz to 0.01 Hz in 0.5 M $Na_2SO_4$ solution.

### 2.4. Electrolytic experiments

The heterogeneous EF tests were performed in a two-chamber electrolysis cell separated by a proton exchange membrane (Nafion 117, DuPont, USA). The electrolytes in both anode and cathode cells were 100 mL solution containing 50 mg/L MIT with 0.1 M $Na_2SO_4$. The prepared $Fe_2O_3$@C/CC and a dimension stable anode (DSA) were used

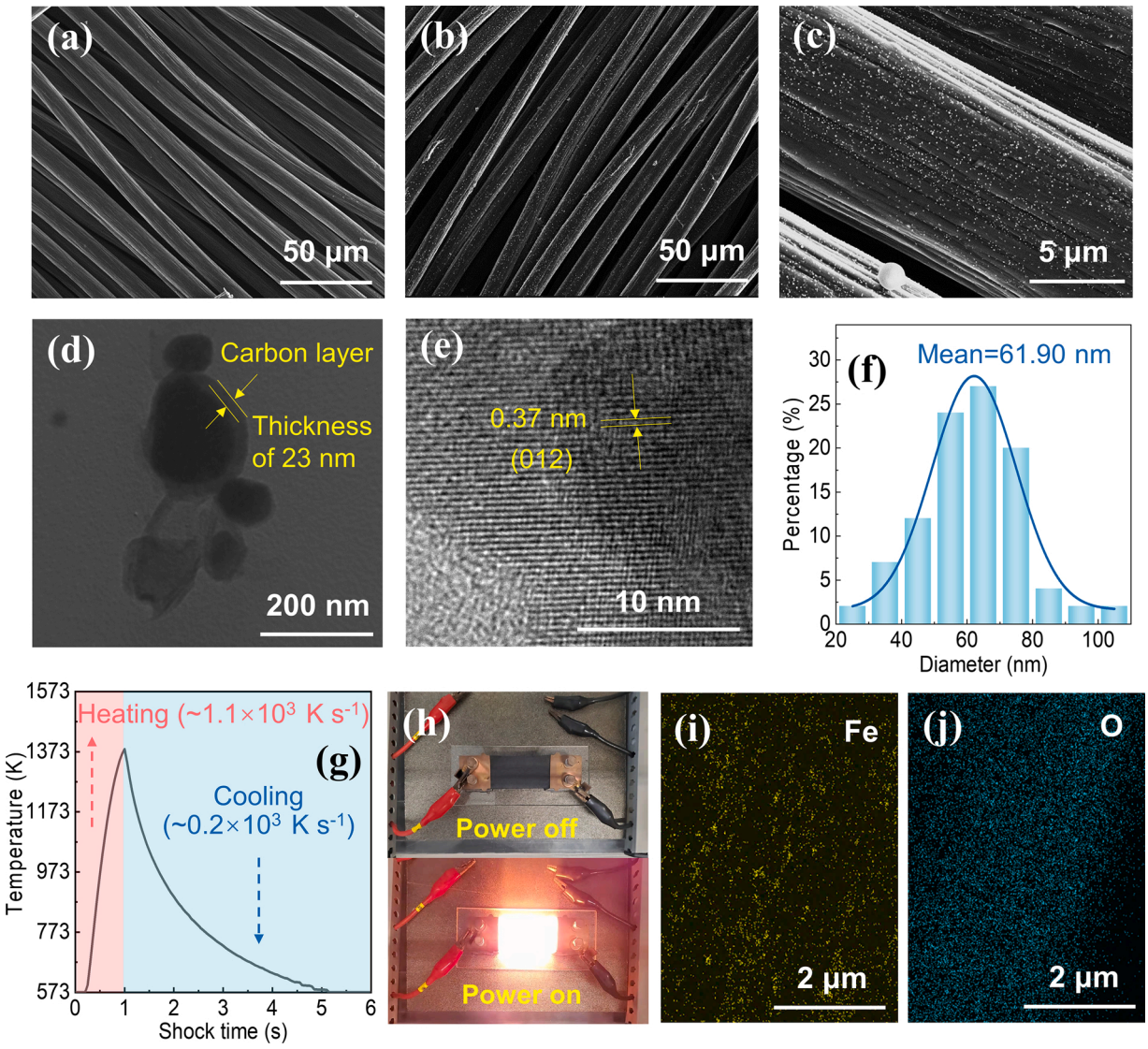


**Fig. 2.** (a) SEM image of CC cathode. (b)–(c) SEM images of $Fe_2O_3$@C/CC cathodes prepared by HTS. (d) TEM image of $Fe_2O_3$@C NPs. (e) HRTEM image of $Fe_2O_3$@C NPs. (f) Particle size distribution of the $Fe_2O_3$@C NPs. (g) Temporal evolution of temperature during the HTS process. (h) Digital photos of cathodes during the HTS process. (i)–(j) EDX mapping of elements in $Fe_2O_3$@C/CC cathode.

as cathode and anode, respectively. The initial pH of the solution was adjusted using $H_2SO_4$ or NaOH. An aeration pump was used to aerate the solution, and the flow rate was regulated by a rotor flowmeter. In order to improve the utilization rate of oxygen, a microporous nano aeration tube was used for aeration, and the cathodes were wrapped around the aeration tube. The current density was controlled by a DC-regulated power supply (RPS60005C-2, Rek). The samples were taken from the cathode chamber at predetermined time points and analyzed to determine the MIT degradation efficiency.

### 2.5. Analytical methods

The concentration of MIT was determined spectroscopically at the wavelength of 273 nm. The $H_2O_2$ concentration was determined by potassium titanium (IV) oxalate spectrophotometry at the wavelength of 400 nm [29].

Based on the previous research, pCBA can react specifically with HO· radicals ($k_{HO\cdot/pCBA} = 5.0 \times 10^9\ M^{-1}\ s^{-1}$) [30]. Therefore, the steady state of HO· concentration can be determined by the degradation rate of pCBA. The time-integrated concentration of HO· concentration was calculated using Eq. (4) [31,32].

$$\int_{t=0}^{t}[HO\cdot]dt = \frac{1}{k_{HO\cdot/pCBA}} ln\left(\frac{[pCBA]_{L,t=0}}{[pCBA]_{L,t}}\right) \quad (4)$$

where $[pCBA]_{L,\,t\,=\,0}$ is the initial concentration of pCBA (2 mg $L^{-1}$), and $[pCBA]_{L,\,t}$ is the concentration at electrolysis time $t$ (mg $L^{-1}$). The pCBA concentration was measured by high-performance liquid chromatography (HPLC, E2695, Waters, USA) with the mobile phase of methanol and aqueous solution of 10 mM phosphoric acid [28].

The degradation intermediates of MIT were identified by liquid chromatograph- mass spectrometer (LC-MS, Thermo scientific Q Exactive, USA, Hypersil gold analytical column) with the mobile phase of methanol and aqueous solution of 0.1% formic acid.

### 2.6. Computational methods

The energy variations during the MIT degradation process were calculated theoretically. Molecular structures of the intermediates were optimized at the Density Functional Thoery (DFT) level (B3LYP/def2scp) by using Python-based simulations of chemistry framework (PySCF) package [33]. The sum of electronic and zero-point energies,

sum of electronic and thermal energies, sum of electronic and thermal enthalpies and sum of electronic and thermal free energies for all the molecules were calculated at the DFT level (B3LYP/6–31 G (d, p)) by using the PySCF package. The implicit solvent model using the dielectric constant of water was applied here considering the solvation influence.

## 3. Results and discussion

### 3.1. Preparation and morphology characterization

The SEM images of CC and $Fe_2O_3$@C/CC cathode are shown in Figs. 2(a)–(c) and Fig. S2. The prepared CC showed a clean fiber structure. After HTS treatment, the iron oxide NPs uniformly dispersed on CC have an average diameter of 61.90 ± 15.09 nm (Fig. 2(f)). The structure of the $Fe_2O_3$@C NPs was further investigated by TEM. As shown in Fig. 2 (d), the $Fe_2O_3$ NPs showed a sphere-like morphology encased in the thin carbon layers with an average thickness of ~23 nm. The TEM samples were prepared via the ultrasonic treatment of the $Fe_2O_3$@C/CC cathode in ethanol for 30 min. The core-shell structure of NPs remained intact after ultrasonic treatment, indirectly confirming that the $Fe_2O_3$@C NPs are firmly confined on the CC with the protection of the carbon layers. The interplanar distance was about 0.37 nm in the results of HRTEM (Fig. 2(e)), which is corresponding to the (012) lattice plane of $Fe_2O_3$.

The CC was soaked in $FeCl_3$ solution and then dried, which was connected to the HTS control system by a pair of conductive graphite clips. An ultra-high temperature laser thermometer was used to record the temperature change during the process. After the power supply was switched on, the temperature of the sample increased rapidly to approximately 1373 K within 1 s at a heating rate of ~$1.1 \times 10^3$ K $s^{-1}$, as shown in Fig. 2(g). Meanwhile, the electrode sample glowed brightly (Fig. 2(h)). After the power was cut off, the sample was cooled down to room temperature at the rate of ~$0.2 \times 10^3$ K $s^{-1}$. In this process, $FeCl_3$ particles were impinged into $Fe_2O_3$ NPs. Thus, the $Fe_2O_3$@C/CC was successfully synthesized through the HTS technique.

The EDX elemental mapping of $Fe_2O_3$@C/CC cathode revealed the distribution of Fe and O elements on the carbon fiber (Fig. 2(i)–(j)). The elemental mapping showed that Fe (yellow) was evenly distributed together with O (cyan), indicating that the doped Fe might exist in an oxidation state. The signal of Cl was not obvious due to the evaporation of the Cl element as chlorine gas in $FeCl_3$ during the HTS process (Fig. S3). Besides, the coexistence of C, Fe, and O was further confirmed by the TEM mapping of $Fe_2O_3$@C NPs (Fig. S4).

### 3.2. Structural and electrochemical characterization

XPS was used to determine the elemental chemical states and surface compositions of $Fe_2O_3$@C/CC, as shown in Fig. 3(a)–(d). The full spectrum further verified the existence of C, Fe, and O elements in $Fe_2O_3$@C/CC (Fig. 3(a)). This is consistent with EDX mapping results. The C 1s peak of $Fe_2O_3$@C/CC can be separated into three distinct peaks (Fig. 3 (b)), including 284.5, 285.4, and 287.1 eV for the $sp^2$ hybridization of carbon atoms, C–O, and C=O species, individually [14,34–35]. For the O 1s spectrum (Fig. 3(c)), three typical peaks could be clearly identified (marked as O1, O2, and O3). The O1 peak at 530.3 eV belongs to lattice oxygen ($O^{2-}$), representing the bounding of oxygen atoms to metals [36]. The O2 peak located at 531.8 eV is indexed to defect sites of oxygen, which is beneficial in regulating the chemical structure and electronic structure of its surface [22]. The O3 peak at 533.3 eV belongs to the absorbed water molecule on the surface [16,37]. As shown in Fig. 3(d), the Fe species contained $Fe^{3+}$ $2p_{3/2}$(711.0 eV), $Fe^{3+}$ $2p_{1/2}$(724.7 eV), and satellite peaks (715.8 and 730.9 eV) [37–39]. This finding is consistent with the characteristic peak of ferric oxide ($Fe_2O_3$).

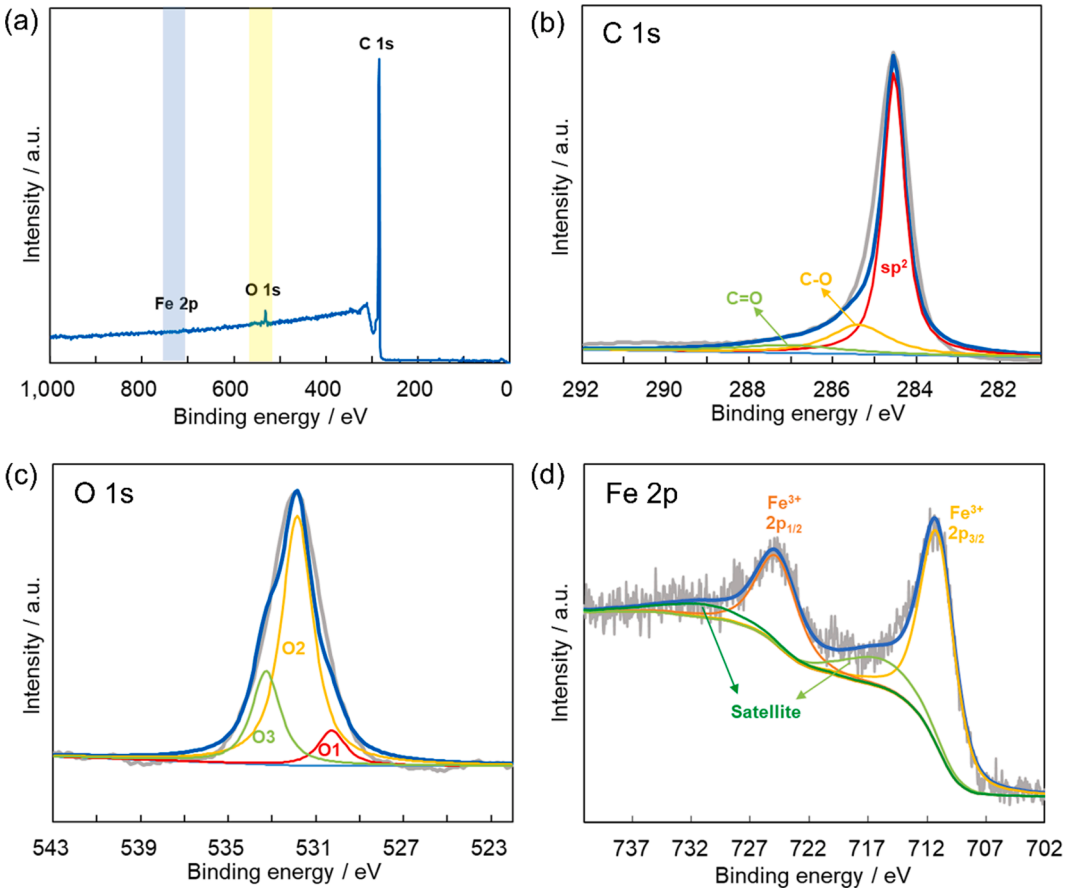


**Fig. 3.** XPS spectra of (a) survey scan, (b) C 1s, (c) O 1s, and (d) Fe 2p for $Fe_2O_3$@C/CC.

The above results indicate that the as-prepared electrode is $Fe_2O_3$ NPs loaded on CC.

LSV curves were used to evaluate the electrocatalytic activity of the cathode. As shown in Fig. 4(a), the current of $Fe_2O_3$@C/CC cathode is more responsive than that of CC, implying that $Fe_2O_3$@C is beneficial in improving the ORR activity [40]. As shown in Fig. 4(b), the reduction peak current and area values of $Fe_2O_3$@C/CC increased comparing with those of pure CC, indicating that the presence of iron catalyst improves the electrochemical activity of the electrode [40–41]. EIS is an efficient tool for investigating the interfacial electrochemical performance of electrocatalytic material and its electron transferring ability [22,42]. In Nyquist plots, the compressed semicircular arc and the oblique line represent the cooperative control process of charge transfer and diffusion in the redox reaction process, respectively [34,43–45]. As depicted in Fig. 4(c), the Nyquist plot of $Fe_2O_3$@C/CC exhibits a smaller semicircle diameter than that of CC, indicating that $Fe_2O_3$@C/CC has a small charge transfer resistance. This scenario should be due to the addition of Fe element, which improves the charge transfer capacity of the cathode and increases the surface reaction rate. In addition, CA measurement was conducted to estimate the stability of cathodes (Fig. 4(d)). The currents of both $Fe_2O_3$@C/CC and CC remained stable after running for 1000 s, indicating the excellent electrocatalytic stability of these cathodes. The above results indicate that the electrochemical performance and catalytic activity of $Fe_2O_3$@C/CC cathodes synthesized via HTS technique are improved than those of the pure CC.

### 3.3. Advantage of HTS technique for cathode synthesis

In this work, the innovative HTS technique was used for the first time to prepare the heterogeneous EF cathode. Compared with other synthesis methods for heterogeneous EF cathodes, the HTS technique possesses several advantages, as displayed in Fig. 5(b) and Table S1. Firstly, the HTS technique features ultrafast heating or cooling rate ($10^3$ K $s^{-1}$) (Fig. 5(a)), and the material treatment can be completed within an ultrashort time (*i.e.*, a few seconds or even milliseconds), which is highly efficient. Moreover, the cathode materials prepared via HTS method show ultrafine nanocatalyst size, uniform distribution, excellent material properties, and superior electrochemical performance. In addition, the HTS technique applies joule heat generated by current or voltage pulses to treat materials. This method is undoubtedly more energy-efficient and eco-friendly than traditional ovens or muffle furnaces. Furthermore, the HTS technique has universal applicability to various precursors (*e.g.*, metal salt solution and micron solid particles) and substrate materials (*e.g.*, carbon-based materials and other conductive materials) [20]. In this study, the HTS technique, featured with rapid reaction, high efficiency, low cost, and environmental friendliness, can be applied in preparing electrocatalytic cathodes.

### 3.4. Heterogeneous EF catalytic activity

The heterogeneous EF catalytic activities of the prepared $Fe_2O_3$@C/CC cathodes are studied by several groups of experiments under different operating conditions. As revealed in Fig. 6(a), the removal efficiency of pollutant MIT reached 90.60 ± 1.70% within 40 min as a result of EF reaction for $Fe_2O_3$@C/CC cathode. The removal efficiency of MIT was conspicuously higher than that of the original CC under the same conditions. A small amount of MIT could also be degraded by CC without metal catalyst, possibly because of the advanced metal-free electrochemical oxidation process [50–52]. The reaction rate constant of MIT degradation for $Fe_2O_3$@C/CC cathode in the first 30 min fit with the pseudo-first-order kinetic model.

The effects of current, aeration rate, and initial MIT concentration on degradation performance are further explored. As shown in Fig. 6(b), the removal efficiency of MIT increased gradually with the applied current

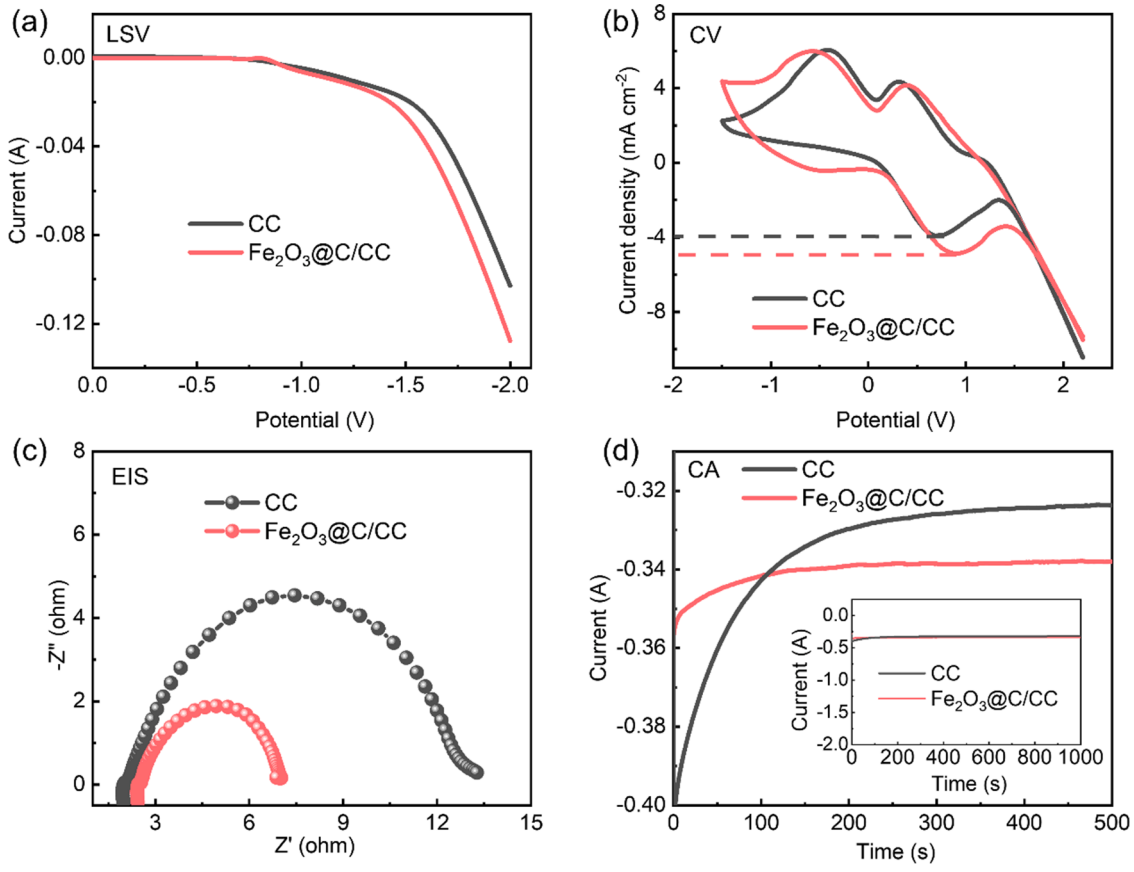


**Fig. 4.** (a) LSV curves, (b) CV curves, (c) Nyquist plots and (d) CA curves of $Fe_2O_3$@C/CC (red) and CC (black).

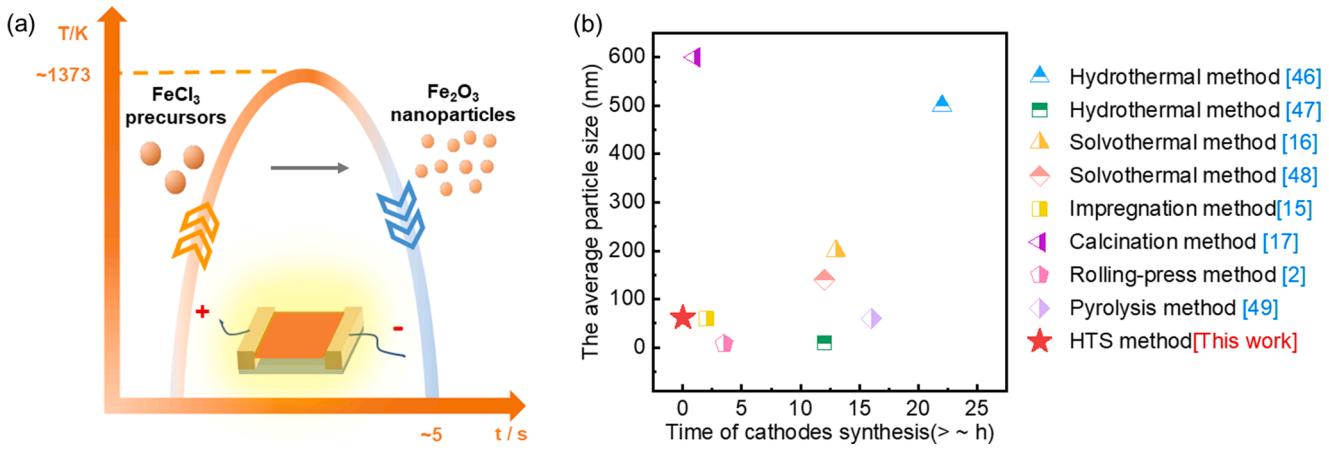


**Fig. 5.** (a) Schematic diagram of $Fe_2O_3$@C/CC cathode synthesis using HTS technique. (b) Comparison of different methods for electrocatalytic cathodes synthesis[46–49].

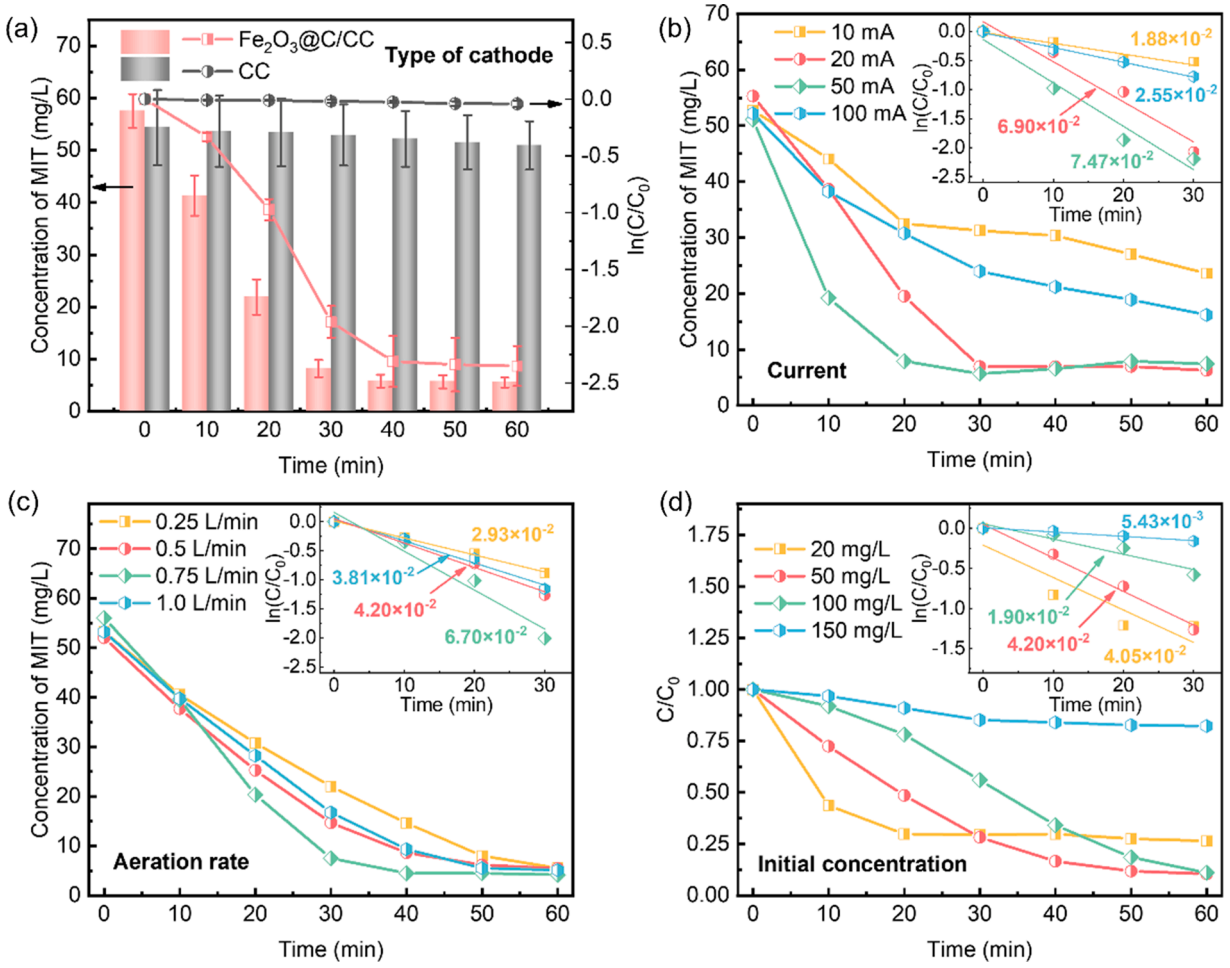


**Fig. 6.** Effect of different operational factors on electrochemical degradation of MIT and corresponding reaction kinetic: (a) type of cathode, (b) current, (c) aeration rate, and (d) initial MIT concentration. Except for the investigated factors above, the reaction conditions are as follows: for $Fe_2O_3$@C/CC cathode, the current applied is 20 mA, pH value is approximately 3.0, aeration rate is 0.75 L/min, and initial concentration of MIT is approximately 50 mg/L.

from 55.20% at 10 mA to 85.44% at 50 mA (the corresponding current density ranging from 0.56 mA $cm^{-2}$ to 2.78 mA $cm^{-2}$). This observation can be attributed to the fast transfer of electrons accelerated by a high current, which promotes $H_2O_2$ formation and the reduction of $Fe^{3+}$ to $Fe^{2+}$ [53]. However, as the current increased to 100 mA (current density 5.56 mA $cm^{-2}$), MIT degradation efficiency declined. This scenario can be explained by the unwanted side reactions in EF systems, such as hydrogen evolution (Eq. (5)) and the 4-electron pathway of oxygen reduction (Eq. (6)) [16,54].

$$2H^+ + 2e^- + \rightarrow H_2 \quad (5)$$

$$O_2 + 4H^+ + 4e^- \rightarrow 2H_2O \quad (6)$$

The impacts of aeration rate are presented in Fig. 6(c). The removal efficiency of MIT could reach 90.51 ± 1.40% after 60 min reaction when the aeration rate ranged from 0.25 L/min to 1.0 L/min. According to Eq. (1), a high concentration of $O_2$ is beneficial for $H_2O_2$ generation and can further enhance the HO· formation. However, excessive aeration interfered with mass transfer between HO· and MIT when the aeration rate was increased to 1.0 L/min [55]. Moreover, an extra high air supply could induce the oxidization of $Fe^{2+}$ to $Fe^{3+}$, hindering the EF reaction (Eq. (2)).

As presented in Fig. 6(d), the removal efficiency of MIT reached 90.78 ± 2.50% after 60 min reaction with the initial concentrations of 50 mg/L and 100 mg/L. By contrast, the removal efficiency of MIT reduced slightly at the concentration of 20 mg/L, resulting from the unthorough contact with HO· at a low concentration. The removal efficiency also decreased when the initial concentration of MIT was 150 mg/L. This phenomenon was due to the degradation intermediates that competed with MIT for HO· at a high initial concentration.

In conclusion, $Fe_2O_3$@C/CC has excellent MIT removal performance under suitable conditions. In addition, compared to previous studies (Table S2), the heterogeneous EF system with $Fe_2O_3$@C/CC cathode has extremely low energy consumption (0.0667 kWh $g^{-1}$ of MIT) and high current efficiency (79.06 ± 5.36%). The cycle experiments of the $Fe_2O_3$@C/CC electrode for EF degradation of MIT are presented in Fig. S5. MIT removal efficiency can maintain at ~70% after four cycles, which was attributed to the stable nanoparticles under the protection of the carbon shell. SEM and XPS characterization of the used electrodes (Figs. S6 and S7) revealed that the surface nanoparticles were partially shed in the acidic solution after several cycles, but the chemical properties of the catalysts remained basically stable. It will be vital to explore more effective methods to reduce metal dissolution and improve the stability of the cathodes in the future.

### 3.5. Reaction mechanism of heterogeneous EF

The reaction mechanism of heterogeneous EF was discussed by analyzing the production of $H_2O_2$ and HO·. According to Eq. (1), $H_2O_2$ production is inhibited in the absence of aeration. Thus, the degradation of MIT in EF reaction was limited by dissolved oxygen in solution without aeration, as shown in Fig. 7(a) (blue line). Fig. 7(a) also indicates that $H_2O_2$ or $O_2$ alone cannot degrade MIT without electricity (purple line and green line). The EF reaction occurs only when both aeration and electricity are applied (red line). Moreover, the addition of $H_2O_2$ improved the degradation rate because the added $H_2O_2$ helped skip the ORR. The Fenton reaction was performed directly to speed up the reaction process (yellow line).

As a precursor of HO·, $H_2O_2$ plays a key role in EF reaction. The yield of $H_2O_2$ directly determines the yield of HO· and further affects the reaction rate of the whole system. The accumulation of $H_2O_2$ electrogenerated in the solution is shown in Fig. 7(b). In particular, $H_2O_2$ concentration did not change considerably when $H_2O_2$ was added manually in the absence of electricity (purple line). This behavior is mainly due to the fact that $Fe^{3+}$ cannot complete the cycle with $Fe^{2+}$ while without electricity. Therefore, it cannot maintain the continuous EF reaction. This finding is consistent with the results in Fig. 7(a). The

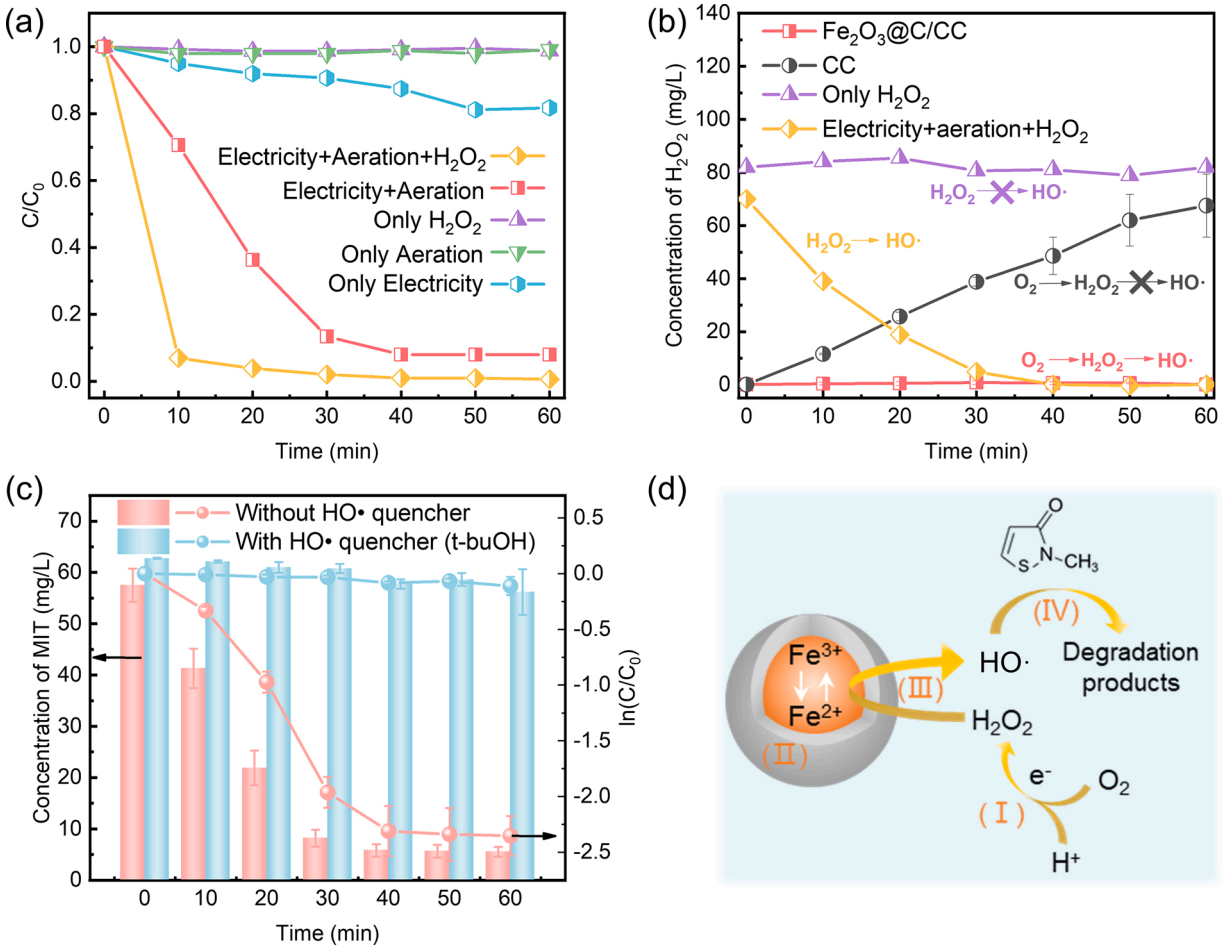


**Fig. 7.** Reaction mechanism in EF system. (a) Electrochemical degradation of MIT under different conditions. (b) $H_2O_2$ concentration accumulation under different conditions. (c) Electrochemical degradation of MIT with HO· quencher. (d) The diagram of the heterogeneous EF reaction process. ("$H_2O_2$" in Fig. 7(a) means external $H_2O_2$ was added to the system. Concentrations of $H_2O_2$ and t-buOH added externally are approximately 80 mg/L and 5 M, respectively.).

externally added $H_2O_2$ was quickly consumed and catalyzed by $Fe^{2+}$ to form HO· (yellow line). For the CC cathode, $H_2O_2$ was generated according to the reaction in Eq. (1). $H_2O_2$ concentration reached 67.52 ± 11.89 mg/L at 60 min (black line). However, the $H_2O_2$ generated by ORR was nearly exhausted in the $Fe_2O_3$@C/CC system (red line); that is, a large amount of electrogenerated $H_2O_2$ was decomposed *in situ* into HO· as a result of EF reaction (Eq. (2)).

T-buOH was used as the HO· quencher to explore the role of HO· in

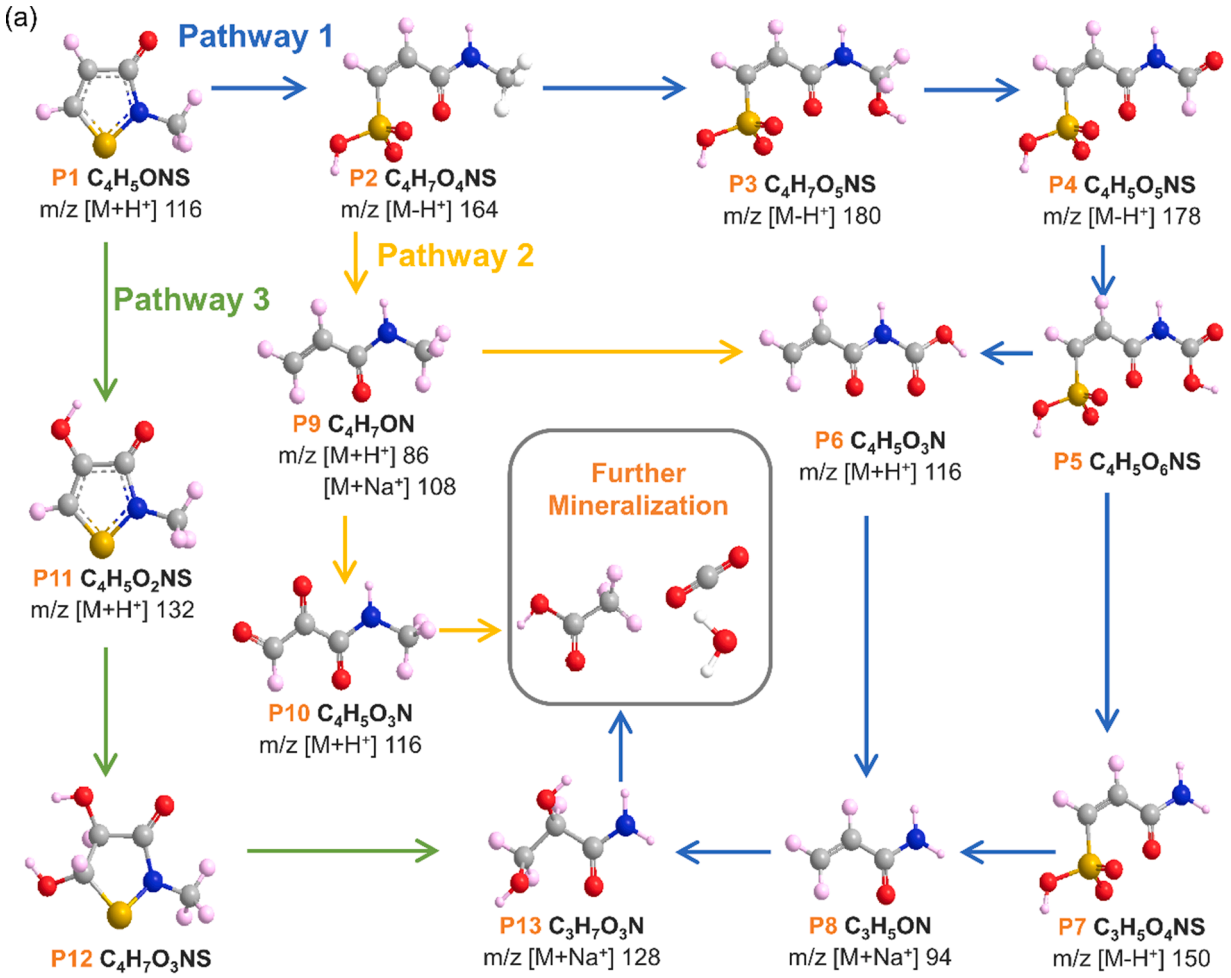


**Fig. 8.** (a) Proposed degradation pathways of MIT. (b) Energy variation of different degradation pathways.

this system indirectly. In the presence of t-buOH, the MIT removal efficiency using $Fe_2O_3$@C/CC cathode dropped sharply (Fig. 7(c)). This value is nearly the same as the removal efficiency of the CC cathode. The results demonstrate that the HO· produced by $Fe_2O_3$@C/CC is the main active radical species to degrade MIT. These results are also confirmed by Fig. S8. HO· exposure was calculated using Eq. (4) based on the degradation of pCBA in the cathode chamber. Compared with CC cathode, more pCBA could be degraded by $Fe_2O_3$@C/CC cathode. The HO· generation rate of $Fe_2O_3$@C/CC cathode was much higher than that of CC. Therefore, $Fe_2O_3$@C/CC is a great heterogeneous EF cathode material with an outstanding performance of producing $H_2O_2$ and then converting it into HO·.

As shown in Fig. 7(d), the reaction process in the heterogeneous EF system is summarized as follows based on the above analysis: (I) Gaseous and dissolved $O_2$ is diffused to the solid–liquid interface of the cathode and subsequently reduced to $H_2O_2$ with the assistance of $H^+$ (according to Eq. (1))[56]. (II) The iron species on the cathode surface are cyclically transformed by gaining or losing electrons [57], as described in Eq. (3). (III) $Fe^{2+}$ catalyzes the conversion of $H_2O_2$ to HO· as the primary active sites initiating the Fenton reaction (Eq. (2)). (IV) HO· with nonselective oxidation capacity degrades MIT.

### 3.6. Proposed degradation pathway of MIT

The degradation intermediates of MIT were detected by LC-MS, as displayed in Fig. S9 and Table S3. The possible three degradation pathways of MIT are shown in Fig. 8(a). Pathway 1 (blue line): The –S–N– bond of MIT was broken and the heterocyclic ring was opened firstly. The S atom in the MIT molecule is a typical electron-rich group, so it is easily oxidized by electrophiles [58]. Then, the products were oxidized to alcohols, aldehydes, and carboxylic acids. Step by step, the carboxyl and S atoms on the products were stripped away. Pathway 2 (yellow line): After the heterocyclic ring was opened, the product was first stripped of S atoms and further oxidized. Pathway 3 (green line): The C=C bond of MIT molecule underwent an addition reaction with HO· generated in the EF reaction. Subsequently, the product continued to be oxidized. In the degradation process of MIT, N atoms remained in the chain organic matter, and S atoms were oxidized. Finally, the intermediates were eventually mineralized to carbon dioxide and water. The above discussion determines that the electrochemical degradation of MIT is a complex and multistep reaction. The proposed three possible pathways can guide the mechanism study of MIT degradation and other related electrochemical reactions.

Molecule energy variations of intermediates in different degradation pathways are shown in Fig. 8(b). In Pathway 1, the –S–N– bond was the preferred active site to be attacked during the MIT degradation process. In general, a negative change in Gibbs free energy is considered a spontaneous reaction. Moreover, the reaction tends to go in the direction of releasing more energy [59]. The path of P5–P6–P8 (decarboxylation followed by desulphurization) had a slight advantage compared with P5–P7–P8 (desulphurization followed by decarboxylation). This may be due to that –COOH is more stable than $–HSO_3$ in the P5 molecules. Pathway 2 differs from Pathway 1 in that the molecule was desulphurized before forming the carboxyl group. This process could also happen spontaneously, except for the oxidation of the C=C bond in the step of P9–P10. For Pathway 3, the first reaction coordinate was the C=C bond. C=C bond underwent an addition reaction and was subsequently degraded into molecules such as P13 through a series of processes including desulfurization and decarboxylation. On the downside, the addition reaction required a lot of energy to occur in this process. Therefore, of the three pathways proposed, Pathway 1 is the most advantageous. In other words, the dominant degradation pathway of MIT in the heterogeneous EF system is heterocyclic opening at the –S–N– bond first and further mineralization to small molecules.

## 4. Conclusions

In this work, we fabricated $Fe_2O_3$@C/CC cathode via the HTS technique for heterogeneous EF systems. The as-prepared cathode was carefully characterized regarding morphology, structure, property, and electrochemical performance. It was applied for the EF degradation of a typical organic pollutant (*i.e.*, MIT, a common biocide). The results indicated that the degradation efficiency of $Fe_2O_3$@C/CC for MIT could approach $90.60 \pm 1.70\%$ within 40 min under optimal conditions of the applied current of 20 mA and aeration rate of 0.75 L/min. The $H_2O_2$ production and mechanism analysis further confirmed that HO· is the dominant active component to degrade MIT during the EF process. During degradation, MIT was oxidized by HO· into small molecules (*e.g.*, carboxylic acids) and eventually mineralized into carbon dioxide and water. Combined with the results of theoretical calculation, heterocyclic loop opening is the main pathway of MIT degradation. Finally, the present study provides a rapid and eco-friendly alternative for cathode preparation with outstanding activity and stability for the heterogeneous EF process. The proposed possible pathways for MIT degradation can inspire the mechanism study of related electrochemical reactions.

## CRediT authorship contribution statement

**Shuang Pan:** Investigation, Formal analysis, Methodology, Writing – original draft. **Chang Liu:** Investigation, Methodology. **Yanchao Li:** Investigation, Visualization. **Can Wang:** Supervision, Funding acquisition, Resources, Writing – review & editing. **Xiaoya Cui:** Writing – review & editing. **Ning Liu:** Validation. **Cong Zhang:** Validation. **Israel Hakizimana:** Validation. **Xin Zhao:** Supervision. **Weidi Liu:** Writing – review & editing. **Yanan Chen:** Supervision, Resources, Writing – review & editing.

## Declaration of Competing Interest

The authors declare that they have no known competing financial interests or personal relationships that could have appeared to influence the work reported in this paper.

## Data Availability

No data was used for the research described in the article.

## Acknowledgment

The authors acknowledge funding from the the Key Technologies R&D Program of Tianjin (21JCZDJC00580).

## Supplementary materials

Supplementary material associated with this article can be found, in the online version, at doi:10.1016/j.electacta.2022.141262.

## References

[1] L. Ma, M. Zhou, G. Ren, W. Yang, L. Liang, A highly energy-efficient flow-through electro-Fenton process for organic pollutants degradation, Electrochim. Acta 200 (2016) 222–230, https://doi.org/10.1016/j.electacta.2016.03.181.
[2] P. Su, M. Zhou, G. Ren, X. Lu, X. Du, G. Song, A carbon nanotube-confined iron modified cathode with prominent stability and activity for heterogeneous electro-Fenton reactions, J. Mater. Chem. A 7 (2019) 24408–24419, https://doi.org/10.1039/c9ta07491k.
[3] L. Xie, X. Mi, Y. Liu, Y. Li, Y. Sun, S. Zhan, W. Hu, Highly efficient degradation of polyacrylamide by an Fe-doped $Ce_{0.75}Zr_{.25}O_2$ solid solution/CF composite cathode in a heterogeneous electro-Fenton process, ACS Appl. Mater. Interfaces 11 (2019) 30703–30712, https://doi.org/10.1021/acsami.9b06396.
[4] Y. Jiao, L. Ma, Y. Tian, M. Zhou, A flow-through electro-Fenton process using modified activated carbon fiber cathode for orange II removal, Chemosphere 252 (2020), 126483, https://doi.org/10.1016/j.chemosphere.2020.126483.

[5] T. Hu, L. Tang, H. Feng, J. Zhang, X. Li, Y. Zuo, Z. Lu, W. Tang, Metal-organic frameworks (MOFs) and their derivatives as emerging catalysts for electro-Fenton process in water purification, Coord. Chem. Rev. 451 (2022), 214277, https://doi.org/10.1016/j.ccr.2021.214277.

[6] E. Brillas, I. Sirés, M.A. Oturan, Electro-Fenton process and related electrochemical technologies based on Fenton's reaction chemistry, Chem. Rev. 109 (2009) 6570–6631, https://doi.org/10.1021/cr900136g.

[7] J.J. Aaron, M.A. Oturan, New photochemical and electrochemical methods for the degradation of pesticides in aqueous media. Environmental applications, Turk. J. Chem. 25 (4) (2001) 509–520. https://journals.tubitak.gov.tr/chem/vol25/iss4/15.

[8] M. El Kateb, C. Trellu, A. Darwich, M. Rivallin, M. Bechelany, S. Nagarajan, S. Lacour, N. Bellakhal, G. Lesage, M. Heran, M. Cretin, Electrochemical advanced oxidation processes using novel electrode materials for mineralization and biodegradability enhancement of nanofiltration concentrate of landfill leachates, Water Res. 162 (2019) 446–455, https://doi.org/10.1016/j.watres.2019.07.005.

[9] J.M. Peralta-Hernandez, Y. Meas-Vong, F.J. Rodríguez, T.W. Chapman, M. I. Maldonado, L.A. Godínez, *In situ* electrochemical and photoelectrochemical generation of the Fenton reagent: a potentially important new water treatment technology, Water Res. 40 (2006) 1754–1762, https://doi.org/10.1016/j.watres.2006.03.004.

[10] Y.S. Jung, W.T. Lim, J.Y. Park, Y.H. Kim, Effect of pH on Fenton and Fenton-like oxidation, Environ. Technol. 30 (2009) 183–190, https://doi.org/10.1080/09593330802468848.

[11] E. Rosales, O. Iglesias, M. Pazos, M.A. Sanroman, Decolourisation of dyes under electro-Fenton process using Fe alginate gel beads, J. Hazard. Mater. 213 (2012) 369–377, https://doi.org/10.1016/j.jhazmat.2012.02.005.

[12] T. Luo, H. Feng, L. Tang, Y. Lu, W. Tang, S. Chen, J. Yu, Q. Xie, X. Ouyang, Z. Chen, Efficient degradation of tetracycline by heterogeneous electro-Fenton process using Cu-doped Fe@ $Fe_2O_3$: mechanism and degradation pathway, Chem. Eng. J. 382 (2020), 122970, https://doi.org/10.1016/j.cej.2019.122970.

[13] D. Kubo, Y. Kawase, Hydroxyl radical generation in electro-Fenton process with *in situ* electro-chemical production of Fenton reagents by gas-diffusion-electrode cathode and sacrificial iron anode, J. Clean. Prod. 203 (2018) 685–695, https://doi.org/10.1016/j.jclepro.2018.08.231.

[14] S. Cheng, C. Shen, H. Zheng, F. Liu, A. Li, OCNTs encapsulating Fe-Co PBA as efficient chainmail-like electrocatalyst for enhanced heterogeneous electro-Fenton reaction, Appl. Catal. B Environ. 269 (2020), 118785, https://doi.org/10.1016/j.apcatb.2020.118785.

[15] J. Li, Z. Ai, L. Zhang, Design of a neutral electro-Fenton system with Fe@ $Fe_2O_3$/ACF composite cathode for wastewater treatment, J. Hazard. Mater. 164 (2009) 18–25, https://doi.org/10.1016/j.jhazmat.2008.07.109.

[16] L. Cui, Z. Li, Q. Li, M. Chen, W. Jing, X. Gu, Cu/$CuFe_2O_4$ integrated graphite felt as a stable bifunctional cathode for high-performance heterogeneous electro-Fenton oxidation, Chem. Eng. J. 420 (2021), 127666, https://doi.org/10.1016/j.cej.2020.127666.

[17] H. Tang, Z. Zhu, Q. Shang, Y. Tang, D. Zhang, Y. Du, M. Liu, K. Yin, C. Liu, Highly efficient continuous-flow electro-Fenton treatment of antibiotic wastewater using a double-cathode system, ACS Sustain. Chem. Eng. 9 (2021) 1414–1422, https://doi.org/10.1021/acssuschemeng.0c08705.

[18] P. Wu, Y. Zhang, Z. Chen, Y. Duan, Y. Lai, Q. Fang, F. Wang, S. Li, Performance of boron-doped graphene aerogel modified gas diffusion electrode for *in-situ* metal-free electrochemical advanced oxidation of Bisphenol A, Appl. Catal. B Environ. 255 (2019), 117784, https://doi.org/10.1016/j.apcatb.2019.117784.

[19] H. Lan, J. Li, M. Sun, X. An, C. Hu, R. Liu, H. Liu, J. Qu, Efficient conversion of dimethylarsinate into arsenic and its simultaneous adsorption removal over $FeC_x$/N-doped carbon fiber composite in an electro-Fenton process, Water Res. 100 (2016) 57–64, https://doi.org/10.1016/j.watres.2016.05.018.

[20] S. Dou, J. Xu, X. Cui, W. Liu, Z. Zhang, Y. Deng, W. Hu, Y. Chen, High-temperature shock enabled nanomanufacturing for energy-related applications, Adv. Eng. Mater. 10 (2020), 2001331, https://doi.org/10.1002/aenm.202001331.

[21] S. Liu, Y. Shen, Y. Zhang, B. Cui, S. Xi, J. Zhang, L. Xu, S. Zhu, Y. Chen, Y. Deng, W. Hu, Extreme environmental thermal shock induced dislocation-rich Pt nanoparticles boosting hydrogen evolution reaction, Adv. Mater. 34 (2022), 2106973, https://doi.org/10.1002/adma.202106973.

[22] C. Liu, W. Zhou, J. Zhang, Z. Chen, S. Liu, Y. Zhang, J. Yang, L. Xu, W. Hu, Y. Chen, Y. Deng, Air-assisted transient synthesis of metastable nickel oxide boosting alkaline fuel oxidation reaction, Adv. Eng. Mater. 10 (2020), 2001397, https://doi.org/10.1002/aenm.202001397.

[23] Y. Chen, G.C. Egan, J. Wan, S. Zhu, R.J. Jacob, W. Zhou, J. Dai, Y. Wang, V. A. Danner, Y. Yao, K. Fu, Y. Wang, W. Bao, T. Li, M.R. Zachariah, L. Hu, Ultra-fast self-assembly and stabilization of reactive nanoparticles in reduced graphene oxide films, Nat. Commun. 7 (2016) 12332, https://doi.org/10.1038/ncomms12332.

[24] Y. Chen, Y. Li, Y. Wang, K. Fu, V.A. Danner, J. Dai, D.L. Steven, Y. Yao, L. Hu, Rapid, *in situ* synthesis of high capacity battery anodes through high temperature radiation-based thermal shock, Nano Lett. 16 (2016) 5553–5558, https://doi.org/10.1021/acs.nanolett.6b02096.

[25] Y. Li, Y. Chen, A. Nie, A. Lu, R.J. Jacob, T. Gao, J. Song, J. Dai, J. Wan, G. Pastel, M.R. Zachariah, R.S. Yassar, L. Hu, *In situ*, fast, high-temperature synthesis of nickel nanoparticles in reduced graphene oxide matrix, Adv. Eng. Mater. 7 (2017), 1601783, https://doi.org/10.1002/aenm.201601783.

[26] V. Kandavelu, H. Kastien, K.R. Thampi, Photocatalytic degradation of isothiazolin-3-ones in water and emulsion paints containing nanocrystalline $TiO_2$ and ZnO catalysts, Appl. Catal. B Environ. 48 (2004) 101–111, https://doi.org/10.1016/j.apcatb.2003.09.022.

[27] F.C. Devos, L. Pollaris, S. Van Den Broucke, S. Seys, A. Goossens, B. Nemery, H.M. H. Peter, A.J.V. Jeroen, Methylisothiazolinone: dermal and respiratory immune responses in mice, Toxicol. Lett. 235 (2015) 179–188, https://doi.org/10.1016/j.toxlet.2015.04.009.

[28] M. Chen, C. Wang, Y. Wang, X. Meng, Z. Chen, W. Zhang, G. Tan, Kinetic, mechanism and mass transfer impact on electrochemical oxidation of MIT using Ti-enhanced nanotube arrays/$SnO_2$-Sb anode, Electrochim. Acta 323 (2019), 134779, https://doi.org/10.1016/j.electacta.2019.134779.

[29] R.M. Sellers, Spectrophotometric determination of hydrogen peroxide using potassium titanium (IV) oxalate, Analyst 105 (1980) 950–954, https://doi.org/10.1039/AN9800500950.

[30] M.S. Elovitz, U. von Gunten, Hydroxyl radical/ozone ratios during ozonation processes. I. The $R_{ct}$ concept, Ozone Sci. Eng. 21 (1999) 239–260, https://doi.org/10.1080/01919519908547239.

[31] Y. Wang, M. Chen, C. Wang, X. Meng, W. Zhang, Z. Chen, J. Crittenden, Electrochemical degradation of methylisothiazolinone by using Ti/$SnO_2$-$Sb_2O_3$/α, β-$PbO_2$ electrode: kinetics, energy efficiency, oxidation mechanism and degradation pathway, Chem. Eng. J. 374 (2019) 626–636, https://doi.org/10.1016/j.cej.2019.05.217.

[32] M. Chen, S. Pan, C. Zhang, C. Wang, W. Zhang, Z. Chen, X. Zhao, Y. Zhao, Electrochemical oxidation of reverse osmosis concentrates using enhanced $TiO_2$-NTA/$SnO_2$-Sb anodes with/without $PbO_2$ layer, Chem. Eng. J. 399 (2020), 125756, https://doi.org/10.1016/j.cej.2020.125756.

[33] Q. Sun, T.C. Berkelbach, N.S. Blunt, G.H. Booth, S. Guo, Z. Li, J. Liu, J.D. McClain, E.R. Sayfutyarova, S. Sharma, S. Wouters, G.K.L. Chan, PySCF: the python-based simulations of chemistry framework, WIRES Comput. Mol. Sci. 8 (2018) e1340, https://doi.org/10.1002/wcms.1340.

[34] P. Dong, X. Chen, M. Guo, Z. Wu, H. Wang, F. Lin, J. Zhang, S. Wang, C. Zhao, H. Sun, Heterogeneous electro-Fenton catalysis with self-supporting CFP@ $MnO_2$-$Fe_3O_4$/C cathode for shale gas fracturing flowback wastewater, J. Hazard. Mater. 412 (2021), 125208, https://doi.org/10.1016/j.jhazmat.2021.125208.

[35] Q. Tian, F. Xiao, H. Zhao, X. Fei, X. Shen, G. Postole, G. Zhao, Simultaneously accelerating the regeneration of $Fe^{II}$ and the selectivity of $2e^-$ oxygen reduction over sulfide iron-based carbon aerogel in electro-Fenton system, Appl. Catal. B Environ. 272 (2020), 119039, https://doi.org/10.1016/j.apcatb.2020.119039.

[36] A.A. Nada, B.O. Orimolade, H.H. El-Maghrabi, B.A. Koiki, M. Rivallin, M.F. Bekhee, R. Viter, D. Damberga, G. Lesage, I. Iatsunskyi, E. Coy, M. Creti, O.A. Arotib, M. Bechelany, Photoelectrocatalysis of paracetamol on Pd-ZnO/N-doped carbon nanofibers electrode, Appl. Mater. Today 24 (2021), 101129, https://doi.org/10.1016/j.apmt.2021.101129.

[37] H. Xia, Z. Zhang, J. Liu, Y. Deng, D. Zhang, P. Du, S. Zhang, X. Lu, Novel Fe-Mn-O nanosheets/wood carbon hybrid with tunable surface properties as a superior catalyst for Fenton-like oxidation, Appl. Catal. B Environ. 259 (2019), 118058, https://doi.org/10.1016/j.apcatb.2019.118058.

[38] J. Li, J. Miao, X. Duan, J. Dai, Q. Liu, S. Wang, W. Zhou, Z. Shao, Fine-tuning surface properties of perovskites via nanocompositing with inert oxide toward developing superior catalysts for advanced oxidation, Adv. Funct. Mater. 28 (2018), 1804654, https://doi.org/10.1002/adfm.201804654.

[39] B. Zhang, L. Wang, Y. Zhang, Y. Ding, Y. Bi, Ultrathin FeOOH nanolayers with abundant oxygen vacancies on $BiVO_4$ photoanodes for efficient water oxidation, Angew. Chem. Int. Ed. 57 (2018) 2248–2252, https://doi.org/10.1002/anie.201712499.

[40] W. Yang, M. Zhou, N. Oturan, M. Bechelany, M. Cretin, M.A. Oturan, Highly efficient and stable $Fe^{II}Fe^{III}$ LDH carbon felt cathode for removal of pharmaceutical ofloxacin at neutral pH, J. Hazard. Mater. 393 (2020), 122513, https://doi.org/10.1016/j.jhazmat.2020.122513.

[41] B.O. Orimolade, B.N. Zwane, B.A. Koiki, M. Rivallin, M. Bechelany, N. Mabuba, G. Lesag, M. Cretin, O.A. Arotiba, Coupling cathodic electro-Fenton with anodic photo-electrochemical oxidation: a feasibility study on the mineralization of paracetamol, J. Environ. Chem. Eng. 8 (5) (2020), 104394, https://doi.org/10.1016/j.jece.2020.104394.

[42] M. Wen, H. Liu, F. Zhang, Y. Zhu, D. Liu, Y. Tian, Q. Wu, Amorphous FeNiPt nanoparticles with tunable length for electrocatalysis and electrochemical determination of thiols, Chem. Commun. 30 (2009) 4530–4532, https://doi.org/10.1039/B907379E.

[43] L. Shi, S. Liu, Z. He, H. Yuan, J. Shen, Synthesis of boron and nitrogen co-doped carbon nanofiber as efficient metal-free electrocatalyst for the $VO^{2+}$/$VO_2^+$ redox reaction, Electrochim. Acta 178 (2015) 748–757, https://doi.org/10.1016/j.electacta.2015.08.026.

[44] F. Lou, D. Chen, Aligned carbon nanostructures based 3D electrodes for energy storage, J. Energy Chem. 24 (2015) 559–586, https://doi.org/10.1016/j.jechem.2015.08.013.

[45] J. He, L. Luo, Y. Chen, A. Manthiram, Yolk-shelled C@$Fe_3O_4$ nanoboxes as efficient sulfur hosts for high-performance lithium-sulfur batteries, Adv. Mater. 29 (2017), 1702707, https://doi.org/10.1002/adma.201702707.

[46] H. Zhao, Y. Wang, Y. Wang, T. Cao, G. Zhao, Electro-Fenton oxidation of pesticides with a novel $Fe_3O_4$@$Fe_2O_3$/activated carbon aerogel cathode: high activity, wide pH range and catalytic mechanism, Appl. Catal. B Environ. 125 (2012) 120–127, https://doi.org/10.1016/j.apcatb.2012.05.044.

[47] H. Qi, X. Sun, Z. Sun, Cu-doped $Fe_2O_3$ nanoparticles/etched graphite felt as bifunctional cathode for efficient degradation of sulfamethoxazole in the heterogeneous electro-Fenton process, Chem. Eng. J. 427 (2022), 131695, https://doi.org/10.1016/j.cej.2021.131695.

[48] N.T. Dung, N.T. Hoa, V.D. Thao, N.N. Huy, A comprehensive study on the heterogeneous electro-Fenton degradation of tartrazine in water using $CoFe_2O_4$/

carbon felt cathode, Chemosphere 287 (2022), 132141, https://doi.org/10.1016/j.chemosphere.2021.132141.
[49] C. Zhang, F. Li, R. Wen, H. Zhang, P. Elumalai, Q. Zheng, H. Chen, Y. Yang, M. Huang, G. Ying, Heterogeneous electro-Fenton using three-dimension NZVI-BC electrodes for degradation of neonicotinoid wastewater, Water Res. 182 (2020), 115975, https://doi.org/10.1016/j.watres.2020.115975.
[50] F. Xiao, Z. Wang, J. Fan, T. Majima, H. Zhao, G. Zhao, Selective electrocatalytic reduction of oxygen to hydroxyl radicals via 3-electron pathway with FeCo alloy encapsulated carbon aerogel for fast and complete removing pollutants, Angew. Chem. Int. Ed. 60 (2021) 10375–10383, https://doi.org/10.1002/anie.202101804.
[51] W. Yang, M. Zhou, L. Liang, Highly efficient *in-situ* metal-free electrochemical advanced oxidation process using graphite felt modified with N-doped graphene, Chem. Eng. J. 338 (2018) 700–708, https://doi.org/10.1016/j.cej.2018.01.013.
[52] M.R. Haider, W.L. Jiang, J. Han, H.M.A. Sharif, Y. Ding, H. Cheng, A. Wang, *In-situ* electrode fabrication from polyaniline derived N-doped carbon nanofibers for metal-free electro-Fenton degradation of organic contaminants, Appl. Catal. B Environ. 256 (2019), 117774, https://doi.org/10.1016/j.apcatb.2019.117774.
[53] P. Cao, X. Quan, K. Zhao, S. Chen, H. Yu, J. Niu, Selective electrochemical $H_2O_2$ generation and activation on a bifunctional catalyst for heterogeneous electro-Fenton catalysis, J. Hazard. Mater. 382 (2020), 121102, https://doi.org/10.1016/j.jhazmat.2019.121102.
[54] L. Cui, H. Huang, P. Ding, S. Zhu, W. Jing, X. Gu, Cogeneration of $H_2O_2$ and •OH via a novel $Fe_3O_4$/MWCNTs composite cathode in a dual-compartment electro-Fenton membrane reactor, Sep. Purif. Technol. 237 (2020), 116380, https://doi.org/10.1016/j.seppur.2019.116380.
[55] P. Xu, D. Zheng, Z. Xie, J. Ma, J. Yu, B. Hou, The mechanism and oxidation efficiency of bio-electro-Fenton system with Fe@$Fe_2O_3$/ACF composite cathode, Sep. Purif. Technol. 234 (2020), 116103, https://doi.org/10.1016/j.seppur.2019.116103.
[56] T. Hu, F. Deng, H. Feng, J. Zhang, B. Shao, C. Feng, W. Tang, L. Tang, Fe/Co bimetallic nanoparticles embedded in MOF-derived nitrogen-doped porous carbon rods as efficient heterogeneous electro-Fenton catalysts for degradation of organic pollutants, Appl. Mater. Today 24 (2021), 101161, https://doi.org/10.1016/j.apmt.2021.101161.
[57] J. Zhang, S. Qiu, H. Feng, T. Hu, Y. Wu, T. Luo, W. Tang, D. Wang, Efficient degradation of tetracycline using core–shell Fe@$Fe_2O_3$-$CeO_2$ composite as novel heterogeneous electro-Fenton catalyst, Chem. Eng. J. 428 (2022), 131403, https://doi.org/10.1016/j.cej.2021.131403.
[58] A. Li, Q. Wu, G. Tian, H. Hu, Effective degradation of methylisothiazolone biocide using ozone: kinetics, mechanisms, and decreases in toxicity, J. Environ. Manag. 183 (2016) 1064–1071, https://doi.org/10.1016/j.jenvman.2016.08.057.
[59] S.P. Devi, R.H.D. Lyngdoh, Uncatalyzed gas phase aziridination of alkenes by organic azides. Part 2. Whole azide reaction with alkene, J. Chem. Sci. 131 (2019) 1–6, https://doi.org/10.1007/s12039-018-1575-4.